GEOLOGY | THE GEOLOGICAL SOCIETY OF AMERICA®

https://doi.org/10.1130/G45479.1

Manuscript received 11 August 2018
Revised manuscript received 4 October 2018
Manuscript accepted 5 October 2018

A dolomitization event at the oceanic chemocline during the Permian-Triassic transition

Mingtao Li[1], Haijun Song[1]*, Thomas J. Algeo[1,2,3], Paul B. Wignall[4], Xu Dai[1], and Adam D. Woods[5]
[1]State Key Laboratory of Biogeology and Environmental Geology, School of Earth Science, China University of Geosciences, Wuhan 430074, China
[2]State Key Laboratory of Geological Processes and Mineral Resources, School of Earth Science, China University of Geosciences, Wuhan 430074, China
[3]Department of Geology, University of Cincinnati, Cincinnati, Ohio 45221-0013, USA
[4]School of Earth and Environment, University of Leeds, Leeds LS2 9JT, UK
[5]Department of Geological Sciences, California State University, Fullerton, California 92834-6850, USA

ABSTRACT

The Permian-Triassic boundary (PTB) crisis caused major short-term perturbations in ocean chemistry, as recorded by the precipitation of anachronistic carbonates. Here, we document for the first time a global dolomitization event during the Permian-Triassic transition based on Mg/(Mg + Ca) data from 22 sections with a global distribution representing shallow- to deep-marine environments. Ten of these sections show high Mg/(Mg + Ca) ratios bracketing the PTB, recording a short-term spike in dolomite formation. The dolomite consists mainly of micron-scale anhedral to subhedral crystals that are associated with abundant fossilized bacterial bodies and extracellular polymeric substances, suggesting that dolomite precipitation was induced by microbial metabolic activity. Sections showing a dolomite spike at the PTB are widely distributed geographically, but mostly encountered in mid-shelf to upper-slope settings. Because the dolomitization event coincided with a rapid expansion of oceanic anoxia and high rates of sulfate reduction, we hypothesize that it was triggered by enhanced microbial sulfate reduction within the oceanic chemocline.

INTRODUCTION

The Permian-Triassic boundary (PTB) crisis, representing the largest mass extinction of the Phanerozoic (Erwin, 2007; Song et al., 2013), was linked to major perturbations of the ocean-atmosphere system, including increases in pCO_2 and large fluctuations in oceanic alkalinity and carbonate saturation levels (Payne and Kump, 2007; Retallack and Jahren, 2008). Changes in the seawater carbonate system are reflected in the widespread precipitation of "anachronistic" carbonates, e.g., microbialites, synsedimentary seafloor cements, ooids, and pisoids (e.g., Baud et al., 2005; Kershaw et al., 2012; Woods, 2014) and in controversial evidence for localized chemical erosion of marine carbonates (Payne and Kump, 2007). PTB oceans were also influenced by concurrent changes in seawater temperatures (Sun et al., 2012), pH values (Clarkson et al., 2015), and redox conditions (Wignall and Twitchett, 2002; Elrick et al., 2017; Zhang et al., 2018a, 2018b).

One aspect of oceanic conditions during the PTB crisis that has received little attention to date is dolomite formation rates. An increase in dolomite in the uppermost Permian–lowermost Triassic was first noted by Wignall and Twitchett (2002) and has been attributed to an increased weathering flux of Mg-bearing clays to the ocean (Algeo et al., 2011). Here, we examine the distribution of dolomite in 22 PTB sections, documenting a global dolomitization event and identifying additional controls on its formation during the Permian-Triassic transition. Our data set shows that mid-depth sections experienced the largest increase in dolomite formation, suggesting the important influence of redox conditions, in addition to seawater alkalinity and Mg concentrations.

MATERIALS AND METHODS

We studied 22 widely distributed PTB sections, including 10 from the eastern Tethys (South China craton), four from the southern Tethys (northern Gondwana margin), five from the western Tethys, and three from Panthalassa (Fig. 1A; Fig. DR1 in the GSA Data Repository[1]). Based on sedimentary characteristics (see details in the Data Repository), these sections were grouped into three environmental categories (Fig. 1B): (1) microbialite-dominated shallow-shelf sections at water depths <~30 m, (2) deep-shelf to slope sections at water depths of ~30–300 m, and (3) deep-basinal sections at water depths >~300 m.

A total of 2034 carbonate samples, including 544 from shallow-shelf sections, 1189 from deep-shelf to slope sections, and 271 from deep-basinal sections (Figs. DR2–DR4), were analyzed by X-ray fluorescence (XRF) or inductively coupled plasma–optical emission spectrometry (ICP-OES) to determine their Mg/(Mg + Ca) ratios. The analytical precision is better than 1% of reported values based on replicate analyses. Our composite Mg/(Mg + Ca) record extends from the middle Permian to the Middle Triassic.

We measured 26 PTB dolostone samples from seven sections (Table DR1) in the southern Tethys, eastern Tethys, and Panthalassa regions for carbon and oxygen isotopes using a Thermo Scientific GasBench II–MAT253 at the State Key Laboratory of Biogeology and Environmental Geology (China University of Geosciences, Wuhan). Results were corrected based on the NBS 19 limestone standard and reported in per mil (‰) relative to the Vienna Pee Dee belemnite (V-PDB) standard; replicate analyses yielded a <0.1‰ error.

---

[1] GSA Data Repository item 2018396, geological background, additional supplemental information, and data (Datasets DR1 and DR2), is available online at http://www.geosociety.org/datarepository/2018/ or on request from editing@geosociety.org.

*E-mail: haijunsong@cug.edu.cn; haijun.song@aliyun.com

CITATION: Li, M., et al., 2018, A dolomitization event at the oceanic chemocline during the Permian-Triassic transition: Geology, v. 46, p. 1043–1046, https://doi.org/10.1130/G45479.1

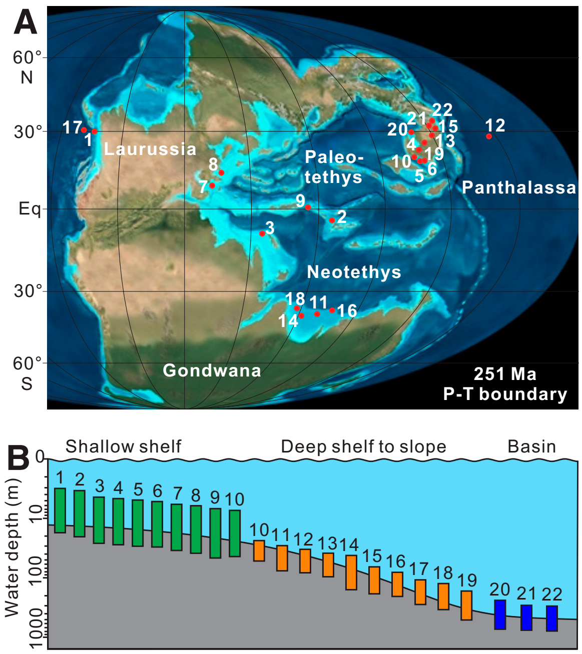

Figure 1. A: Paleogeography of world at the Permian-Triassic (P-T) boundary (PTB) and location of sections used in this study. Eq—equator. Base map courtesy of Ron Blakey (http://jan.ucc.nau.edu/~rcb7/). B: Estimated water-depth range at PTB of study sections; water depth information is from Shen et al. (2015) and Xiao et al. (2017). Note that section 10 is divided into two parts: the lower part corresponding to shallow inner shelf, the remainder to deeper shelf. Studied sections: 1—Jesmond (UK); 2—Zal (Iran); 3—Demirtas (Turkey); 4—Cili (China); 5—Lung Cam (Vietnam); 6—Nhi Tao (Vietnam); 7—Sovetashen (Armenia); 8—Balvany (Hungary); 9—Kurdistan (Iraq); 10—Zuodeng (China); 11—Selong (Tibet); 12—Kamura (Japan); 13—Yangou (China); 14—Spiti (India); 15—Meishan (China); 16—Tulong (Tibet); 17—Ursula Creek (Canada); 18—Guryul Ravine (India); 19—Daxiakou (China); 20—Shangsi (China); 21—South Majiashan (China); 22—West Pingdingshan (China).

RESULTS

For most shallow-shelf sections, Mg/(Mg + Ca) ratios are consistently low in the Changhsingian (uppermost Permian) and Griesbachian (lowermost Triassic), having mean values of 0.02 ± 0.06 ($n = 47$) and 0.03 ± 0.07 ($n = 347$), respectively (Fig. 2). Two sections, Cili and Zuodeng (China), yield modestly higher mean Mg/(Mg + Ca) values (0.10 ± 0.11; $n = 64$) in the lower Griesbachian (Fig. 3B). Two other sections representing peritidal settings, Zal (Iran) and Jesmond (UK), show consistently low Mg/(Mg + Ca) values (mean 0.01 ± 0.01; $n = 55$) from the Changhsingian to the Smithian. Mean Mg/(Mg + Ca) for sections from evaporitic settings rise sharply to 0.39 ± 0.12 ($n = 123$) at the base of the Spathian (Fig. 3A).

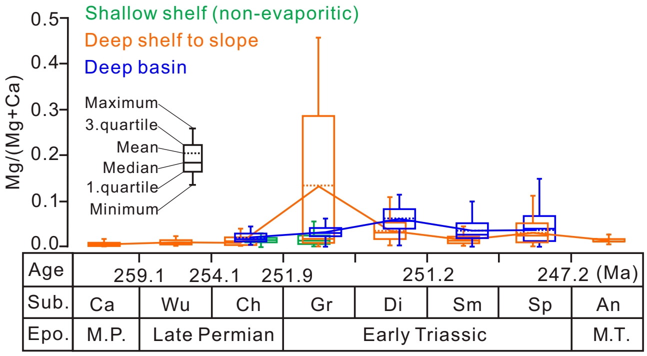

Figure 2. Statistical bar chart of Mg/(Mg + Ca) ratio from middle Permian to Middle Triassic; note that higher values at Permian-Triassic boundary are found in inner- to deep-shelf sections. Abbreviations: Sub.—substage/stage; Ca—Capitanian; Wu—Wuchiapingian; Ch—Changhsingian; Gr—Griesbachian; Di—Dienerian; Sm—Smithian; Sp—Spathian; An—Anisian; Epo.—epoch; M.P.—Middle Permian; M.T.—Middle Triassic.

Deep-shelf to slope sections show a prominent Mg/(Mg + Ca) peak across the PTB (Fig. 2). Mg/(Mg + Ca) ratios are consistently low in the Capitanian (middle Permian; mean 0.01 ± 0.01, $n = 50$), Wuchiapingian (late Permian; mean 0.01 ± 0.02, $n = 70$), and Changhsingian (mean 0.02 ± 0.04, $n = 134$). Mean Mg/(Mg + Ca) climbs to 0.13 ± 0.16 ($n = 249$) in the Griesbachian, drops to 0.07 ± 0.13 ($n = 175$) in the Dienerian, and then further decreases to 0.01–0.04 from the Smithian to the Anisian ($n = 115$). High Mg/(Mg + Ca) ratios (e.g., mean values >0.10) are present across the PTB in all deep-shelf to slope sections except for Guryul Ravine (India) (Fig. 3C). In the Dienerian, four sections (Kamura [Japan], Spiti [India], Ursula Creek [Canada], and Zuodeng [China]) yield moderate to high Mg/(Mg + Ca) ratios (mean 0.09 ± 0.15, $n = 115$), but only one section (Zuodeng) yields high Mg/(Mg + Ca) in the early Smithian (mean 0.22 ± 0.13, $n = 19$).

Deep-basinal sections exhibit slight variations in Mg/(Mg + Ca) ratios in the uppermost Permian–Lower Triassic (Fig. 2). Mean Mg/(Mg + Ca) ratios are 0.02 ± 0.04 ($n = 83$) and 0.03 ± 0.03 ($n = 55$) in the Changhsingian and Griesbachian respectively, peak at 0.06 ± 0.04 ($n = 34$) in the Dienerian, and decrease to 0.04 ± 0.05 ($n = 176$) in the Smithian and Spathian (Fig. 3D).

DISCUSSION

Testing for Detrital Input and Diagenetic Influences

Siliciclastic material can influence measured Mg/(Mg + Ca) ratios, and so samples were screened to minimize this effect: (1) all clay-rich samples (Al >4%) were removed; and (2) the remaining samples were checked for detrital influence by cross-plotting Mg and Ca against Al, and if a significant correlation was detected, the detrital fraction of total Mg and Ca was calculated from the regression line and subtracted from total Mg and Ca to yield carbonate Mg and Ca (see Fig. DR5 for examples).

In addition to detrital influences, sediment Mg/(Mg + Ca) ratios may also have been affected by late burial dolomitization. Therefore, dolostone samples that exhibit evidence of late burial diagenesis were excluded in this analysis, such as from the Anisian interval of the Ursula Creek section, in which calcareous and phosphatic nodules are embedded in the dark-gray shales. Moreover, samples from evaporitic environments, such as from the Spathian interval of the Zal (peritidal setting) and Jesmond (lagoonal setting) sections, are not considered to reflect secular variations of dolomite in the open ocean, because a restricted evaporitic environment has an altered water chemistry that is different from that of the open ocean.

Cross-plots of Mn/Sr versus Mg/(Mg + Ca) were used to test whether elevated Mg/(Mg + Ca) values were a product of late burial alternations; the study sections reveal no correlation ($n = 33$, $R^2 = 0.02$; see Fig. DR6), providing no evidence of a link between dolomitization and late burial diagenesis. Dolostones from China show bright cathodoluminescence patterns indicative of Mn(II) incorporation without Fe quenching (Fig. DR7), which is a feature of early suboxic diagenesis associated with organogenic dolomite (Mazzullo, 2000).

Spatio-Temporal Distribution of PTB Dolomite

Stratigraphically, PTB dolomite peaks are mainly restricted to the lower Griesbachian (Fig. 3C). Among the 10 sections that contain abundant dolomite, nine have dolomite peaks in the *Hindeodus parvus* conodont zone and/or the *Otoceras* ammonoid zone, and one section (Yangou [China]) has a slightly younger peak in the *Isarcicella isarcica* conodont zone. These PTB dolomite peaks followed closely on the Permian-Triassic mass extinction (Song et al., 2013), implying a potential link between these events.

Many of the PTB dolostones are found in sections deposited in deep-shelf to slope settings (Fig. 2). Shallow-shelf settings ($n = 16$) are dominated by microbialites consisting of pure calcium carbonate, according to data from Collin et al. (2015) and this study (see Fig. 3B). In contrast,

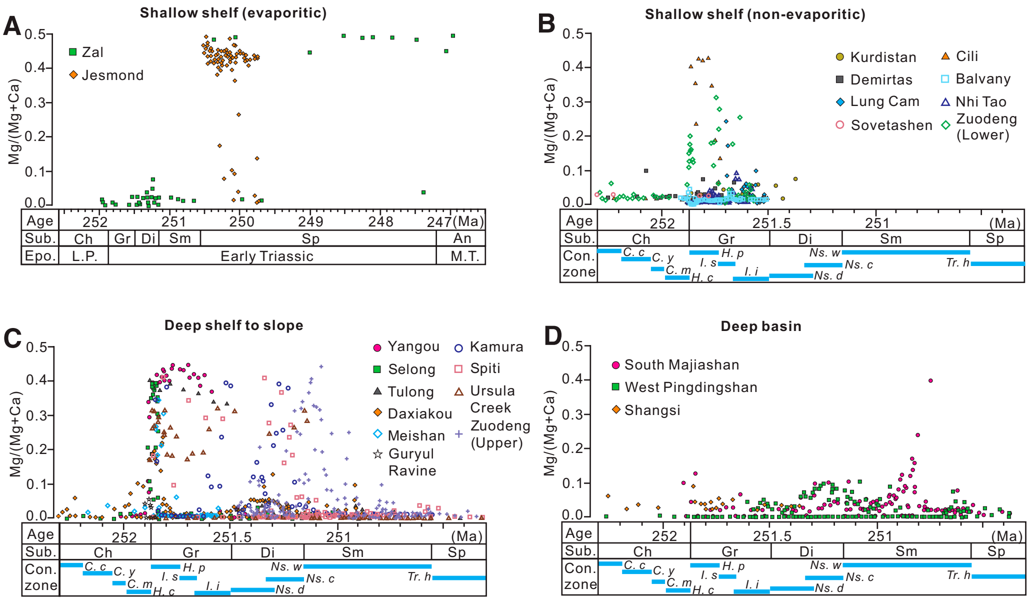

Figure 3. Mg/(Mg + Ca) ratio variation for studied sections (see Fig. 1 for locations). A: Shallow subtidal settings. B: Non-evaporitic shallow-shelf settings. C: Deep-shelf to slope settings. D: Deep-basin settings. Abbreviations: Sub.—substage/stage; Ch—Changhsingian; Gr—Griesbachian; Di—Dienerian; Sm—Smithian; Sp—Spathian; An—Anisian; Epo.—epoch; L.P.—late Permian; M.T.—Middle Triassic; Con.—conodont; *C.c—Clarkina changxingensis*; *C.y—Clarkina yini*; *C.m—Clarkina meishanensis*; *H.c—Hindeodus changxingensis*; *H.p—Hindeodus parvus*; *I.s—Isarcicella staeschei*; *I.i—Isarcicella isarcica*; *Ns.d—Neospathodus dieneri*; *Ns.c—Neospathodus cristagalli*; *Ns.w—Neospathodus waageni*; *Tr.h—Triassospathodus homeri*.

nearly all (eight of nine) sections deposited in deep-shelf to slope settings display a Mg/(Mg + Ca) peak across the PTB (Fig. 3C). For the deepest, basinal sections, Mg/(Mg + Ca) ratios are only slightly higher in the Griesbachian than the Changhsingian (Fig. 3D).

Water-Depth Control on Dolomite Formation and Its Implications

The spatial distribution of facies at the PTB, i.e., microbialite-dominated shallow-shelf, dolostone-dominated deep-shelf, and shale-dominated deep-basin sediments, reveals the influence of water depth on dolomite formation. Dolostones in high-energy shelf settings (e.g., Selong [Tibet], Kamura) are only a few decimeters thick and thicken toward deep-shelf to slope settings (decimeters to meters). These dolostones consist mainly of bioclastic wackestone with a homogenous dolomitic matrix. Overall, dolomite formation was favored by quiet, low-energy shelf settings colonized by abundant sulfate-reducing microbes (Fig. 4A). Associated with these fossilized microbes is dark-gray mineralized organic matter inferred to be extracellular polymeric substances (EPSs) (Fig. 4B).

Secular variations in dolomite abundance have been linked to changes in seawater chemistry, such as changing Mg/Ca ratios and sulfate concentrations (Burns et al., 2000). However, recent experiments have shown that Mg/Ca ratio, SO_4^{2-} concentration, salinity, and pH are of secondary importance compared to microbial activity during dolomite formation (Wright and Wacey, 2005; Krause et al., 2012; Bontognali et al., 2014), suggesting that microbial activity (e.g., sulfate reduction) may have been a key factor in the PTB dolomitization event.

Sulfate-reducing bacteria and associated EPSs have been shown to be critical for the formation of dolomite in numerous experiments (Warthmann et al., 2000; Wright and Wacey, 2005; Bontognali et al., 2014). It is thought that microbial sulfate reduction can overcome the energy barrier to the dehydration of hydrated Mg^{2+} ions and promote dolomite precipitation (Bontognali et al., 2014). The Early Triassic was characterized by

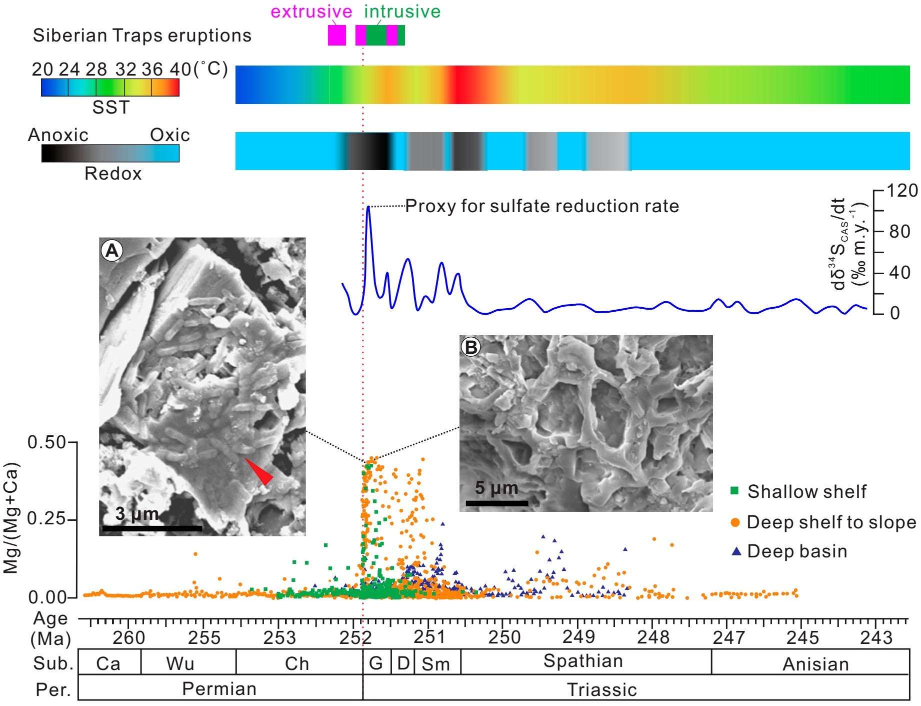

Figure 4. Composite figure showing sharply increased Mg/(Mg + Ca), dramatic ocean sulfate drawdown, intense ocean anoxia, and increased ocean surface temperature at Permian-Triassic boundary. Note abundant fossilized bacteria bodies (red arrow) (A) entombed in dolomite crystal and extracellular polymeric substance displaying alveolar structures (B); sample A is from Selong section (south Tibet) and B is from Meishan section (south China). Ocean sulfate data are after Song et al. (2014); redox conditions are after Song et al. (2012) and Clarkson et al. (2016); temperature data are after Sun et al. (2012); dates for Siberian Traps eruptions are after Burgess et al. (2017). Abbreviations: SST—sea-surface temperature; dt—derivative with respect to time; Sub.—substage/stage; Ca—Capitanian; Wu—Wuchiapingian; Ch—Changhsingian; G—Griesbachian; D—Dienerian; Sm—Smithian; Per.—period.

very hot surface ocean temperatures (Sun et al., 2012), which resulted in an upward shift of the chemocline to inner- to middle-shelf areas, leading to expansion of oceanic anoxia to shallow depths (Wignall and Twitchett, 2002; Grice et al., 2005). The peak of PTB dolomite formation at intermediate water depths was likely the result of microbial sulfate reduction below a relatively shallow oceanic chemocline, a hypothesis supported by U-isotope evidence of expansion of global-ocean anoxia during the earliest Triassic (Zhang et al., 2018a, 2018b).We therefore suggest that enhanced microbial sulfate reduction was an important factor in both sulfate drawdown (Luo et al., 2010; Song et al., 2014) and the widespread dolomite precipitation during the Early Triassic (Fig. 4).

CONCLUSIONS

A total of 2034 Mg/(Mg + Ca) data points from 22 sections provide evidence of a global dolomitization event during the Permian-Triassic transition. The dolomite is composed of micron-scale anhedral to subhedral crystals associated with fossilized bacterial bodies and extracellular polymeric substances. The PTB dolomite spike was concentrated in mid-shelf to upper-slope settings and coincided with the rapid expansion of oceanic anoxia, suggesting that widespread dolomite precipitation may have been induced by microbial sulfate reduction below the chemocline of a shallowly stratified ocean. Such dolomitization events may be manifested in the geological record at other times of widespread ocean anoxia and thus constitute an underexplored phenomenon.

ACKNOWLEDGMENTS

We thank S. Jiang and Y. Zhao for field work assistance; Z. Qiu for laboratory assistance; and L. Tian for discussions. This study is supported by the Strategic Priority Research Program of Chinese Academy of Sciences (grant XDB26000000), the National Natural Science Foundation of China (grants 41821001, 41622207, 41530104, 41661134047), the State Key R&D project of China (grant 2016YFA0601100), and the UK Natural Environment Research Council's Eco-PT project (grant NE/P01377224/1), which is a part of the Biosphere Evolution, Transitions and Resilience (BETR) Program. This study is a contribution to the International Geoscience Programme (IGCP) 630 project. We thank two anonymous reviewers for their constructive comments.

REFERENCES CITED

Algeo, T.J., Kuwahara, K., Sano, H., Bates, S., Lyons, T., Elswick, E., Hinnov, L., Ellwood, B., Moser, J., and Maynard, J.B., 2011, Spatial variation in sediment fluxes, redox conditions, and productivity in the Permian-Triassic Panthalassic Ocean: Palaeogeography, Palaeoclimatology, Palaeoecology, v. 308, p. 65–83, https://doi.org/10.1016/j.palaeo.2010.07.007.

Baud, A., Richoz, S., and Marcoux, J., 2005, Calcimicrobial cap rocks from the basal Triassic units: Western Taurus occurrences (SW Turkey): Comptes Rendus Palevol, v. 4, p. 569–582, https://doi.org/10.1016/j.crpv.2005.03.001.

Bontognali, T.R.R., McKenzie, J.A., Warthmann, R.J., and Vasconcelos, C., 2014, Microbially influenced formation of Mg-calcite and Ca-dolomite in the presence of exopolymeric substances produced by sulphate-reducing bacteria: Terra Nova, v. 26, p. 72–77, https://doi.org/10.1111/ter.12072.

Burgess, S.D., Muirhead, J.D., and Bowring, S.A., 2017, Initial pulse of Siberian Traps sills as the trigger of the end-Permian mass extinction: Nature Communications, v. 8, 164, https://doi.org/10.1038/s41467-017-00083-9.

Burns, S.J., McKenzie, J.A., and Vasconcelos, C., 2000, Dolomite formation and biogeochemical cycles in the Phanerozoic: Sedimentology, v. 47, p. 49–61, https://doi.org/10.1046/j.1365-3091.2000.00004.x.

Clarkson, M.O., Kasemann, S.A., Wood, R.A., Lenton, T.M., Daines, S.J., Richoz, S., Ohnemueller, F., Meixner, A., Poulton, S.W., and Tipper, E.T., 2015, Ocean acidification and the Permo-Triassic mass extinction: Science, v. 348, p. 229–232, https://doi.org/10.1126/science.aaa0193.

Clarkson, M.O., Wood, R.A., Poulton, S.W., Richoz, S., Newton, R.J., Kasemann, S.A., Bowyer, F., and Krystyn, L., 2016, Dynamic anoxic ferruginous conditions during the end-Permian mass extinction and recovery: Nature Communications, v. 7, 12236, https://doi.org/10.1038/ncomms12236.

Collin, P.Y., Kershaw, S., Tribovillard, N., Forel, M.B., and Crasquin, S., 2015, Geochemistry of post-extinction microbialites as a powerful tool to assess the oxygenation of shallow marine water in the immediate aftermath of the end-Permian mass extinction: International Journal of Earth Sciences, v. 104, p. 1025–1037, https://doi.org/10.1007/s00531-014-1125-3.

Elrick, M., Polyak, V., Algeo, T.J., Romaniello, S., Asmerom, Y., Herrmann, A.D., Anbar, A.D., Zhao, L., and Chen, Z.-Q., 2017, Global-ocean redox variation during the middle-late Permian through Early Triassic based on uranium isotope and Th/U trends of marine carbonates: Geology, v. 45, p. 163–166, https://doi.org/10.1130/G38585.1.

Erwin, D.H., 2007, Disparity: Morphological pattern and developmental context: Palaeontology, v. 50, p. 57–73, doi:https://doi.org/10.1111/j.1475-4983.2006.00614.x.

Grice, K., Cao, C., Love, G.D., Böttcher, M.E., Twitchett, R.J., Grosjean, E., Summons, R.E., Turgeon, S.C., Dunning, W., and Jin, Y., 2005, Photic zone euxinia during the Permian-Triassic superanoxic event: Science, v. 307, p. 706–709, https://doi.org/10.1126/science.1104323.

Kershaw, S., Crasquin, S., Li, Y., Collin, P.-Y., Forel, M.-B., Mu, X., Baud, A., Wang, Y., Xie, S., Maurer, F., and Guo, L., 2012, Microbialites and global environmental change across the Permian-Triassic boundary: A synthesis: Geobiology, v. 10, p. 25–47, https://doi.org/10.1111/j.1472-4669.2011.00302.x.

Krause, S., Liebetrau, V., Gorb, S., Sánchez-Román, M., McKenzie, J.A., and Treude, T., 2012, Microbial nucleation of Mg-rich dolomite in exopolymeric substances under anoxic modern seawater salinity: New insight into an old enigma: Geology, v. 40, p. 587–590, https://doi.org/10.1130/G32923.1.

Luo, G., Kump, L.R., Wang, Y., Tong, J., Arthur, M.A., Yang, H., Huang, J., Yin, H., and Xie, S., 2010, Isotopic evidence for an anomalously low oceanic sulfate concentration following end-Permian mass extinction: Earth and Planetary Science Letters, v. 300, p. 101–111, https://doi.org/10.1016/j.epsl.2010.09.041.

Mazzullo, S.J., 2000, Organogenic dolomitization in peritidal to deep-sea sediments: Journal of Sedimentary Research, v. 70, p. 10–23, https://doi.org/10.1306/2DC408F9-0E47-11D7-8643000102C1865D.

Payne, J.L., and Kump, L.R., 2007, Evidence for recurrent Early Triassic massive volcanism from quantitative interpretation of carbon isotope fluctuations: Earth and Planetary Science Letters, v. 256, p. 264–277, https://doi.org/10.1016/j.epsl.2007.01.034.

Retallack, G.J., and Jahren, A.H., 2008, Methane release from igneous intrusion of coal during Late Permian extinction events: The Journal of Geology, v. 116, p. 1–20, https://doi.org/10.1086/524120.

Shen, J., Schoepfer, S.D., Feng, Q., Zhou, L., Yu, J., Song, H., Wei, H., and Algeo, T.J., 2015, Marine productivity changes during the end-Permian crisis and Early Triassic recovery: Earth-Science Reviews, v. 149, p. 136–162, https://doi.org/10.1016/j.earscirev.2014.11.002.

Song, H.J., Wignall, P.B., Tong, J., Bond, D.P.G., Song, H.Y., Lai, X., Zhang, K., Wang, H., and Chen, Y., 2012, Geochemical evidence from bio-apatite for multiple oceanic anoxic events during Permian-Triassic transition and the link with end-Permian extinction and recovery: Earth and Planetary Science Letters, v. 353–354, p. 12–21, https://doi.org/10.1016/j.epsl.2012.07.005.

Song, H.J., Wignall, P.B., Tong, J., and Yin, H., 2013, Two pulses of extinction during the Permian-Triassic crisis: Nature Geoscience, v. 6, p. 52–56, https://doi.org/10.1038/ngeo1649.

Song, H.Y., Tong, J., Algeo, T.J., Song, H.J., Qiu, H., Zhu, Y., Tian, L., Bates, S., Lyons, T.W., Luo, G., and Kump, L.R., 2014, Early Triassic seawater sulfate drawdown: Geochimica et Cosmochimica Acta, v. 128, p. 95–113, https://doi.org/10.1016/j.gca.2013.12.009.

Sun, Y., Joachimski, M.M., Wignall, P.B., Yan, C., Chen, Y., Jiang, H., Wang, L., and Lai, X., 2012, Lethally hot temperatures during the Early Triassic greenhouse: Science, v. 338, p. 366–370, https://doi.org/10.1126/science.1224126.

Warthmann, R., Lith, Y.V., Vasconcelos, C., McKenzie, J.A., and Karpoff, A.M., 2000, Bacterially induced dolomite precipitation in anoxic culture experiments: Geology, v. 28, p. 1091–1094, https://doi.org/10.1130/0091-7613(2000)28<1091:BIDPIA>2.0.CO;2.

Wignall, P.B., and Twitchett, R.J., 2002, Extent, duration, and nature of the Permian-Triassic superanoxic event, *in* Koeberl, C., and MacLeod, K.G., eds., Catastrophic Events and Mass Extinctions: Impacts and Beyond: Geological Society of America Special Paper 356, p. 395–413, https://doi.org/10.1130/0-8137-2356-6.395.

Woods, A.D., 2014, Assessing Early Triassic paleoceanographic conditions via unusual sedimentary fabrics and features: Earth-Science Reviews, v. 137, p. 6–18, https://doi.org/10.1016/j.earscirev.2013.08.015.

Wright, D.T., and Wacey, D., 2005, Precipitation of dolomite using sulphate-reducing bacteria from the Coorong Region, South Australia: Significance and implications: Sedimentology, v. 52, p. 987–1008, https://doi.org/10.1111/j.1365-3091.2005.00732.x.

Xiao, Y., Suzuki, N., and He, W., 2017, Water depths of the latest Permian (Changhsingian) radiolarians estimated from correspondence analysis: Earth-Science Reviews, v. 173, p. 141–158, https://doi.org/10.1016/j.earscirev.2017.08.012.

Zhang, F., Romaniello, S.J., Algeo, T.J., Lau, K.V., Clapham, M.E., Richoz, S., Herrmann, A.D., Smith, H., Horacek, M., and Anbar, A.D., 2018a, Multiple episodes of extensive marine anoxia linked to global warming and continental weathering following the latest Permian mass extinction: Science Advances, v. 4, e1602921, https://doi.org/10.1126/sciadv.1602921.

Zhang, F., Algeo, T.J., Romaniello, S.J., Cui, Y., Zhao, L., Chen, Z.-Q., and Anbar, A.D., 2018b, Congruent Permian-Triassic δ^{238}U records at Panthalassic and Tethyan sites: Confirmation of global-oceanic anoxia and validation of the U-isotope paleoredox proxy: Geology, v. 46, p. 327–330, https://doi.org/10.1130/G39695.1.

Printed in USA